RSC Advances

ROYAL SOCIETY OF CHEMISTRY

www.rsc.org/advances

The excellent photocatalytic synergism of $PbBiO_2Br$/UiO-66-NH_2 composite via multiple coupling effects

Sunfeng Li, Xing Wang, Yanli Xu, Hanbiao Yang, Fengyu Wei*, Xueting Liu*

School of Chemistry and Chemical Engineering, Hefei University of Technology, Anhui Key Laboratory of Controllable Chemical Reaction & Material Chemical Engineering, Hefei 230009, Anhui, China

ABSTRACT : $PbBiO_2Br$/UiO-66-NH_2 composites synthesized by a facile solvothermal method have a core-shell structure with UiO-66-NH_2 forming the shell around a $PbBiO_2Br$ core. Their photocatalytic activities in the degradation of RhodamineB (RhB) dye solution and colorless phenol solution under visible light irradiation were investigated. For both model organic pollutants, the $PbBiO_2Br$/UiO-66-NH_2 composites exhibit higher photocatalytic activity than the pure components. This synergistic effect is due to the high adsorption capacity of UiO-66-NH_2 and the compounding induced an enhanced separation efficiency of photogenerated electron-hole pairs. The composite with 3:2 mass ratio of $PbBiO_2Br$ to $ZrCl_4$ exhibits the highest photocatalytic activity for RhB degradation, in which trapping experiments confirm that the photogenerated holes and $O_2\bullet^-$ radicals are the main active species.

Keywords: UiO-66-NH_2; $PbBiO_2Br$; photocatalysis; synergistic effect

1. Introduction

In recent years, dyes are widely used in the textile, paper and printing industries, so the treatment of dye-containing wastewater is a crucial problem to solve [1-3]. Semiconductor (SC) photocatalysis for the photodegradation of organic dyes in water

has emerged as a renewable technology [4-6].

Up until now, numerous materials which show photocatalytic activity under visible light irradiation have been reported [7-11]. $PbBiO_2Br$ has aroused a growing interest recently, due to its band gap of 2.47 eV and unique layered structure [12, 13]. The assembled $PbBiO_2Br$ nanosheets show excellent photocatalytic activity for organic contaminant degradation under visible light irradiation, which is primarily attributed to the structure and the low recombination rate of charges in the ultrathin nanosheets [14].

Recent research has been focused on metal-organic frameworks (MOFs), which are made of metal clusters linked by organic ligands [15-19]. Due to their uniform but tunable pore size and high specific surface area, MOFs are considered for adsorption [20], storage[21-23], and health care applications [24]. A group at Valencia [25] first synthesized a zirconium(IV)-based MOF (UiO-66-NH_2), which is based on a $Zr_6O_4(OH)_4$ octahedron and a lattice formed by 12-fold connection through a 2-amino-1,4-benzene-dicarboxylate linker. The UiO-66-NH_2 framework is robust and can undergo isoreticular functionalization without losing its high hydrothermal and chemical stability [26]. Shen et al. have shown that UiO-66-NH_2 has high visible light photocatalytic activity for reducing Cr(VI) [27].

It has been found that the combination of two different semiconductors can yield an enhanced photocatalytic activity via a synergistic effect such as more efficient charge separation [28-29]. In this work, $PbBiO_2Br$/UiO-66-NH_2 composites prepared

by a facile solvothermal method exhibit enhanced photocatalytic activity for degradation of both RhB dye solution and colorless phenol solution under visible light by its comparison with the pure components.

2. Experimental

2.1 Materials

Bismuth nitrate pentahydrate, ethanol, lead nitrate, hexadecyl trimethyl ammonium bromide (CTAB), ammonia water, benzoic acid, zirconium tetrachloride, N, N-dimethyl formamide (DMF) and chloroform were supplied from Sinopharm Chemical Reagent Co., Ltd. 2-amino-1,4-benzenedicarboxylic acid was purchased from Tokyo Chemical Industry Co., Ltd. And all of chemicals were used as received without further purification.

2.2. Preparation of catalysts

Assembly ultrathin $PbBiO_2Br$ nanosheets samples were synthesized using a solvothermal method [30]. In a typical procedure, 0.5 mmol $Bi(NO_3)_3 \cdot 5H_2O$ was added into 20 mL of ethanol containing stoichiometric amounts of hexadecyl trimethyl ammonium bromide(CTAB) and $Pb(NO_3)_2$ with continuous stirring, and then 5 mL ammonia water was added into this solution. The mixture solution was stirred for at least 30 min and then poured into a 50 mL Teflon-lined stainless autoclave. The autoclave was heated at 180 ℃ for 12 h under autogenous pressure and then cooled to room temperature. The resulting precipitates were collected and

washed with ethanol and deionized water thoroughly and dried at 70 ℃ in air.

The $PbBiO_2Br$/UiO-66-NH_2 composites were synthesized as UiO-66-NH_2 with different $PbBiO_2Br$ /$ZrCl_4$ ratios [25]. A typical method is as follows: $ZrCl_4$ (0.0848 g, 0.36 mmol), 2-amino-1,4-benzenedicarboxylic acid (0.0656 g，0.036 mmol) and benzoic acid (0.984 g，8.0 mmol) were dissolved in DMF (42 mL). $PbBiO_2Br$ (0.127 g，0.24 mmol) was added into the solution under ultrasonic vibration for 30 min. The mixture was transferred to a stainless steel Teflon-lined autoclave of 50 mL capacity and then maintained at 393K for 24 h. Then, the autoclave was cooled in air to room temperature, and the resulting solid was filtered, repeatedly washed with $CHCl_3$ and dried at room temperature. The prepared composite is called $PbBiO_2Br$ /UiO-66-NH_2 (3:2) where the mass ratio of $PbBiO_2Br$ to $ZrCl_4$ is 3:2. Similarly, when the mass ratio of $PbBiO_2Br$ to $ZrCl_4$ is *x:y,* the composite is named $PbBiO_2Br$ /UiO-66-NH_2(*x:y*).

2.3 Characterization

The morphological analysis of the samples was done using a JEM-2100F field emission transmission electron microscopy (FETEM) equipped with an energy-dispersive X-ray spectrometer (EDS). X-ray diffraction (XRD) patterns of the samples were determined in the range of 2θ=4°-60° on a Rigaku D/max-2500V X-ray diffractometer using Cu-Kα (λ=0.154nm) radiation. N_2 adsorption-desorption (BET) was performed on a Tristar II 3020M surface area and porosity analyzer at 77K. Before the actual measurements, the sample was degassed at 70 ℃ for 3 h. X-ray photoelectron spectroscopy (XPS) was conducted using an ESCALAB250

spectrometer. UV-vis spectra were recorded on a DUV-3700 spectrometer. Photoluminescence emission spectra (PL) were measured on a PL measurement system (Fluorolog Tau-3) with the excitation wavelength of 320 nm.

2.4 Adsorption experiments

The adsorption of dye was measured at ambient pressure and 298 K in the dark. 20 mg of the photocatalyst was added into 100 mL dye aqueous solution (20mg/L) with continuous stirring. Samples were taken at a fixed time, and were filtrated by a 0.22 μm filter. The absorbance of the filtrate was measured using a Shimadzu UV-240 spectrophotometer.

2.5 Photocatalytic experiments

The photocatalytic degradation of dye was measured at ambient pressure and 298 K in a home made photochemical reaction equipment. The light source was a PHILIPS 70 W metal halide lamp (λ < 380 nm was filtered out by a cut off filter). 20 mg photocatalyst was added into 100 mL dye (5 mg/L) aqueous solution. Before irradiation, the suspension was continuously stirred for 12 h in the dark in order to reach adsorption-desorption equilibrium between dye and the photocatalyst. The supernatant liquid was obtained by filtration using 0.22 μm filter and examined on a Shimadzu UV-240 spectrophotometer. For comparison, the photocatalytic activities of UiO-66-NH_2 and $PbBiO_2Br$ were also tested under the same conditions. The degradation of colorless model pollutant phenol (5 mg/L) was also conducted under the identical condition with RhB.

3. Results and Discussion

3.1 Morphology and composition of $PbBiO_2Br$/UiO-66-NH_2 photocatalysts

It can be seen from Fig. 1a and b that pure UiO-66-NH_2 comprises disc-like particles with the particle size in the range of 30-40nm. In $PbBiO_2Br$ /UiO-66-NH_2(3:2), the UiO-66-NH_2 particles are still clearly identifiable and the $PbBiO_2Br$ flakes can be also observed. Although the exact size of the $PbBiO_2Br$ flakes is difficult to estimate from the TEM images, the thickness of the flakes is within the range of 6 to 12 nm. And they exhibit a compact patter, as shown in the TEM image (Fig.1c and d). The lattice fringes of the (101) plane of $PbBiO_2Br$ can be obviously seen in Fig. 1e from which the clear heterojunction interfaces of $PBBiO_2Br$/UiO-66-NH_2 are displayed. These indicate that the $PbBiO_2Br$ nanosheets microcrystallines are in intimate contact with UiO-66-NH_2 particles.

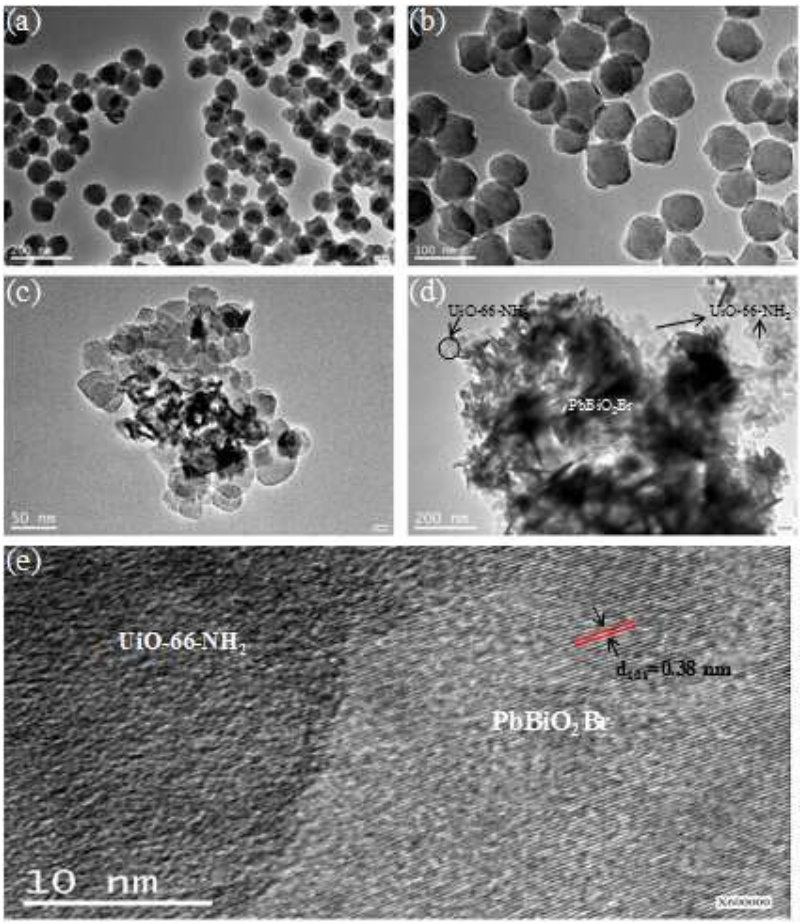

Fig. 1 TEM images of (a and b) UiO-66-NH_2, (c and d) $PbBiO_2Br$/UiO-66-NH_2(3:2), and (e) HRTEM image of $PbBiO_2Br$/UiO-66-NH_2(3:2).

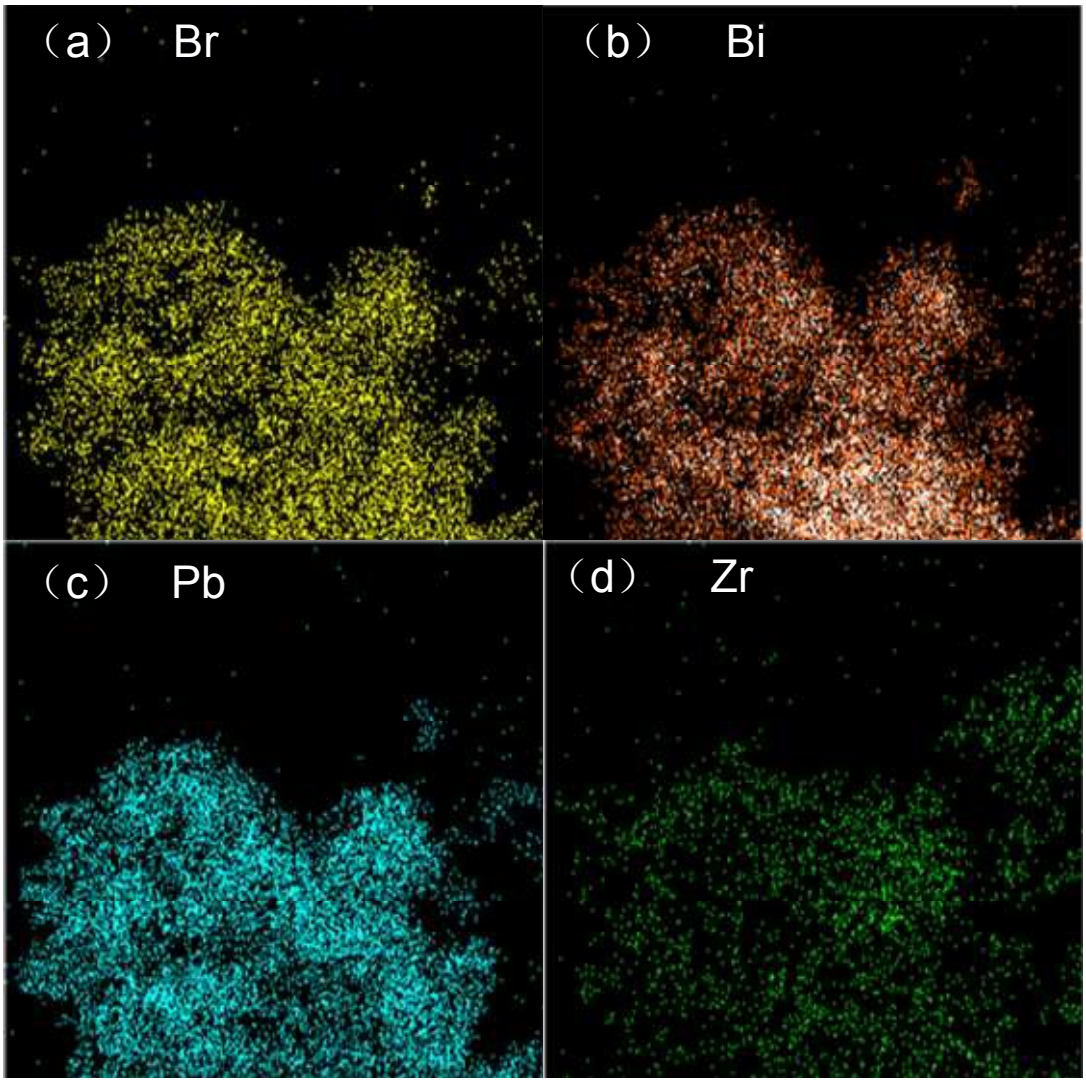

Fig. 2 (a) Br, (b) Bi, (c) Pb and (d) Zr distribution by EDS mapping of $PbBiO_2Br$/UiO-66-NH_2(3:2).

The EDS spectra of $PbBiO_2Br$ /UiO-66-NH_2 (3:2) indicate that Br, Bi, Pb and Zr elements are the major chemical components present in the composite. It can be seen from Fig. 1c and Fig. 2d that $PbBiO_2Br$ and UiO-66-NH_2 exist with the different configurations in the composite. The Br, Bi and Pb distributions by EDS mapping (Fig. 2a, 2b and 2c) show that the flakes are $PbBiO_2Br$ in the composite. However, the

Zr elements are wholly distributed around the flakes as a shell (Fig. 2d). These confirm that the composite possesses a hierarchical core-shell structure with UiO-66-NH_2 forming the shell around the $PbBiO_2Br$ core.

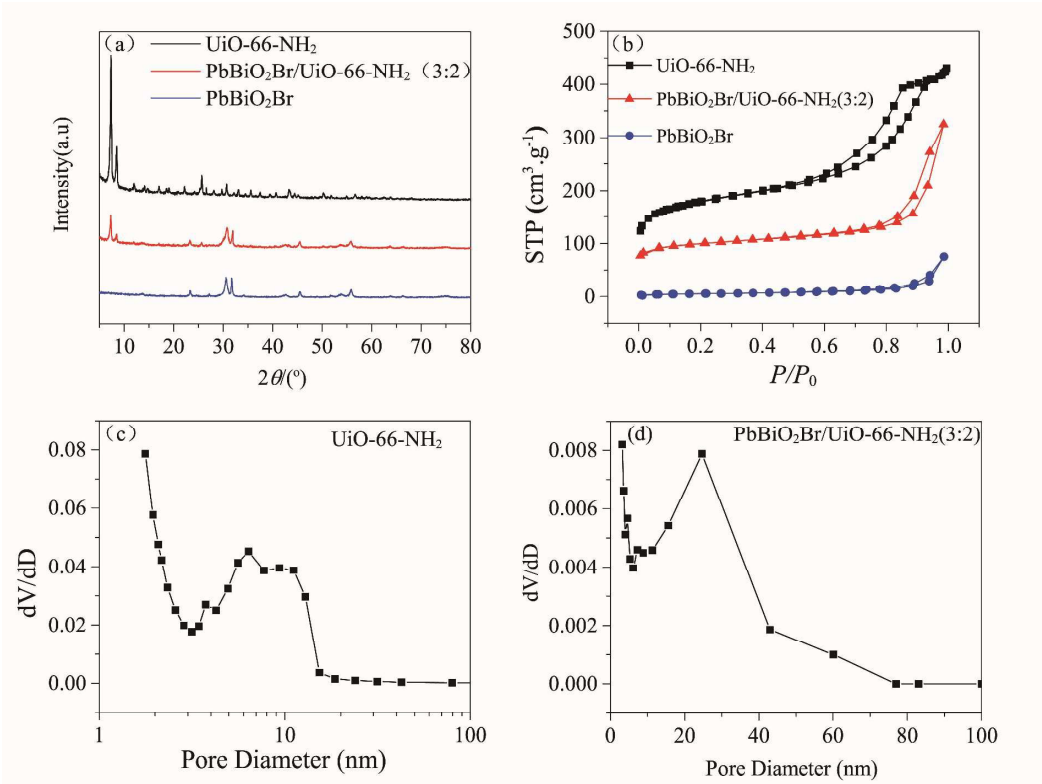

Fig. 3 (a) XRD patterns of UiO-66-NH_2, $PbBiO_2Br$ and $PbBiO_2Br$ /UiO-66-NH_2(3:2); (b) The N_2 adsorption-desorption isotherms of UiO-66-NH_2, $PbBiO_2Br$ and $PbBiO_2Br$ /UiO-66-NH_2(3:2); (c) the BJH pore diameter distribution curve of UiO-66-NH_2; (d) the BJH pore diameter distribution curve of $PbBiO_2Br$ /UiO-66-NH_2(3:2).

The XRD patterns of UiO-66-NH_2, $PbBiO_2Br$ and $PbBiO_2Br$ /UiO-66-NH_2 (3:2) are shown in Fig. 3a, which are in accordance with the reported values [25, 26, 14]. By comparing the XRD patterns of $PbBiO_2Br$ /UiO-66-NH_2 (3:2) with those of the UiO-66-NH_2 and $PbBiO_2Br$ precursors, it can be seen that the composite displays

the characteristic peaks of both UiO-66-NH_2 and $PbBiO_2Br$, and the intensity and location of the peaks are changed somewhat. That is, the composite is not a simple physical mixture, and there exists interfacial interactions between UiO-66-NH_2 and $PbBiO_2Br$.

The N_2 adsorption-desorption isotherms of UiO-66-NH_2, $PbBiO_2Br$ and $PbBiO_2Br$ /UiO-66-NH_2(3:2) are displayed in Fig. 3b, and the values of BET surface area of UiO-66-NH_2, $PbBiO_2Br$ and $PbBiO_2Br$ /UiO-66-NH_2(3:2) are 616.55 m^2/g, 18.14 m^2/g and 320.55 m^2/g, respectively. The N_2 isotherm of UiO-66-NH_2 is categorized as type IV. This property implies the presence of mesopores (between 2 to 50 nm in size). As shown in Figure 3c, the BJH pore size of UiO-66-NH_2 is mainly distributed in the range of 6 to 12 nm, which is attributed to the agglomeration of particles. In contrast, there is no mesopores structure in $PbBiO_2Br$. The surface area of $PbBiO_2Br$ /UiO-66-NH_2 (3:2) is higher than that of pure $PbBiO_2Br$, and its BJH pore diameter distribution is not as homogeneous as in UiO-66-NH_2, but it has even larger pore size. The high surface area and large pore size can enhance the adsorption and reaction for dye molecules on surface active sites. This phenomenon favors for the enhancement in photocatalytic activity.

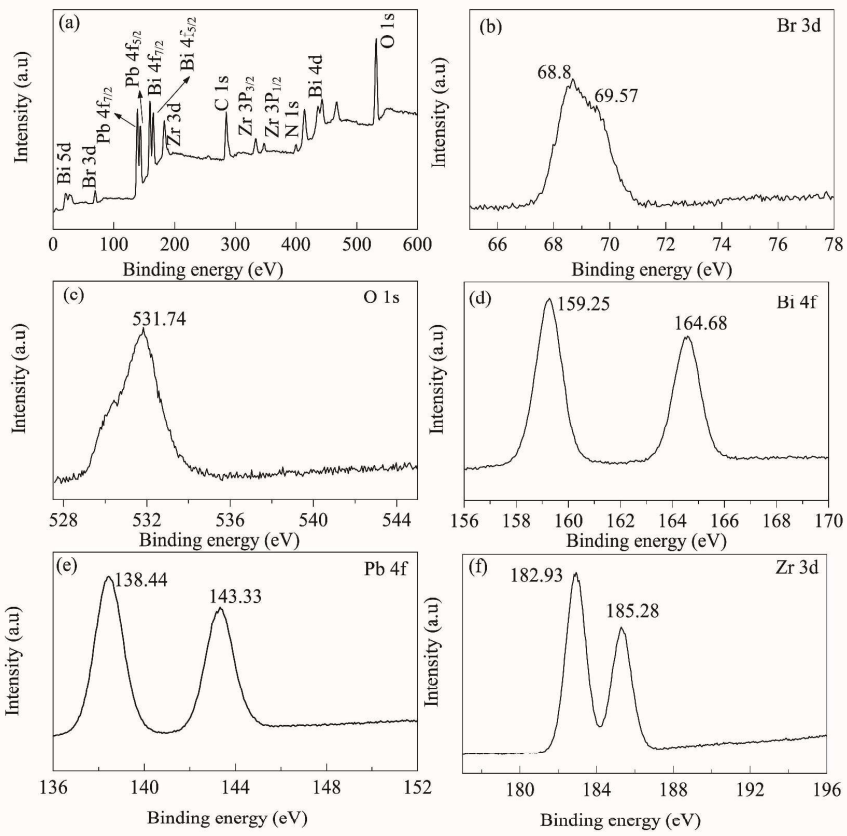

Fig. 4.XPS spectra (a) and high resolution Br 3d (b), O 1s (c), Bi 4f (d), Pb 4f (e) and Zr 3d (f) spectra of $PbBiO_2Br$/UiO-66-NH_2 (3:2).

X-ray photoelectron spectroscopy (XPS) was carried out on the $PbBiO_2Br$/UiO-66-NH_2 (3:2) sample to determine the surface compositions and chemical states of the elements. The shift of the peak position on the charge effect was calibrated by using the binding energy of C1s at 284.78 eV. The survey XPS spectra of $PbBiO_2Br$/UiO-66-NH_2 (3:2) sample are shown in Fig. 4a. Fig. 4b-f show high-resolution XPS spectra of the primary elements. The $Br3d_{5/2}$ and $Br3d_{3/2}$ peaks are associated with the binding energies at 68.8 and 69.57 eV (Fig. 3b). The

asymmetric XPS peak of O1s (Fig. 4c) indicates that oxygen species are present in the form of lattice oxygen and hydroxyl groups adhered onto the surface [31, 18]. Two peaks at 164.68 and 159.25 eV (Fig. 4d) are assigned to $Bi4f_{5/2}$ and $Bi4f_{7/2}$, respectively, which are assigned to Bi^{3+} in the composites [32]. The $Pb4f_{7/2}$ and $Pb4f_{5/2}$ peaks are associated with the binding energies at 138.44 and 143.33 eV (Fig. 4e), respectively. The curves of Zr 3d region could be deconvoluted into two peaks for Zr $3d_{5/2}$ and Zr $3d_{3/2}$ locating at around 182.93 eV and 185.28 eV (Fig. 4f), respectively, which shift to the lower energy compared with the initial UiO-66-NH_2 [26].Therefore, it may be concluded that $PbBiO_2Br$/UiO-66-NH_2 (3:2) heterostructure photocatalysts have been successfully synthesized.

The UV-vis absorption spectra of $PbBiO_2Br$, UiO-66-NH_2 and $PbBiO_2Br$/UiO-66-NH_2 (3:2) were also studied (Fig. 5a). Nanosheet $PbBiO_2Br$ has a strong absorption in the visible range up to 500 nm [30], which is due to the intrinstic transition of the semiconductor. The steep shape rise that UiO-66-NH_2 shows in the range of 300-500 nm is due to the band gap transition [26]. Near the absorption band edge, the optical absorption has the following behavior:

$$\alpha h\nu = A(h\nu - E_g)^{n/2} \quad \text{.....} \quad (1)$$

Where α, ν, Eg, A are absorption coefficient, light frequency, band gap, and a constant, respectively, and n depends on whether the transition is direct (n = 1) or indirect (n = 4) [33]. For UiO-66-NH_2 and $PbBiO_2Br$, the value of n was 1. The band gaps of UiO-66-NH_2 and $PbBiO_2Br$ estimated from the intercept of the tangents to the plots are 2.65 and 2.47 eV, respectively (inset in Figure 5a). As shown in Fig. 5a, the

composite photocatalyst shows the similar absorbance edge to pure UiO-66-NH_2, but its absorbance extends to the visible region due to the presence of $PbBiO_2Br$.

It is well known that PL (photoluminescence emission spectra) can be induced by the recombination between photogenerated electrons and holes. The lower the PL peak is, the less the recombination of electron–hole pairs is. Therefore, PL analysis is often performed to investigate the photogenerated charge separation efficiency. As shown in Figure 5b, the PL emission spectra for samples under excitation at 320 nm were examined in the wavelength range of 340-800 nm, and the order of the PL spectra intensities is as following: UiO-66-NH_2 > $PbBiO_2Br$/ UiO-66-NH_2 (physical mixture) > $PbBiO_2Br$/ UiO-66-NH_2 (3:2) > $PbBiO_2Br$. As indicated, $PbBiO_2Br$ has very low PL spectrum intensity, whereas UiO-66-NH_2 exhibits strong PL spectra. The PL spectrum intensity of $PbBiO_2Br$/ UiO-66-NH_2 (3:2) is lower than that of the corresponding physical mixture, which means the separation of photogenerated electron-hole pairs is enhanced for the $PbBiO_2Br$/ UiO-66-NH_2 (3:2) binary composite.

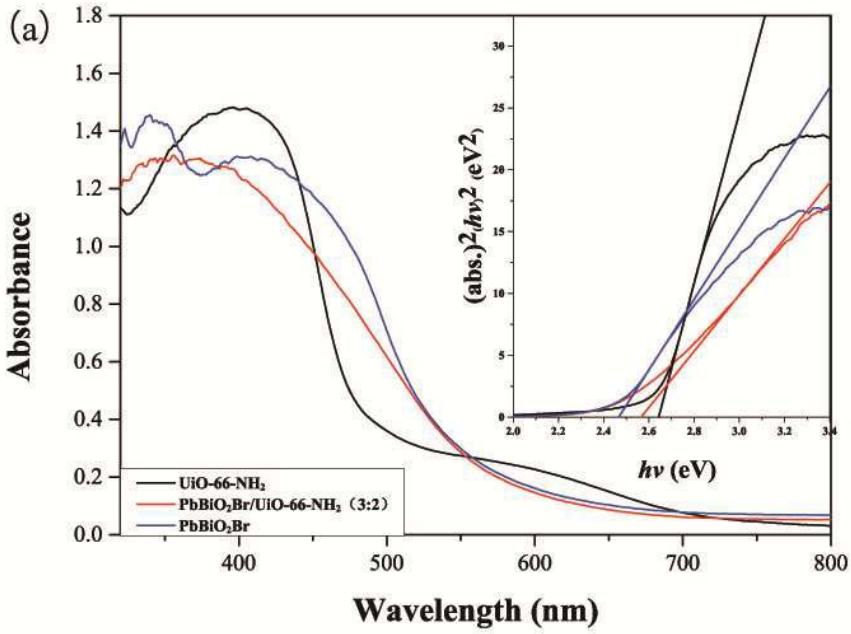

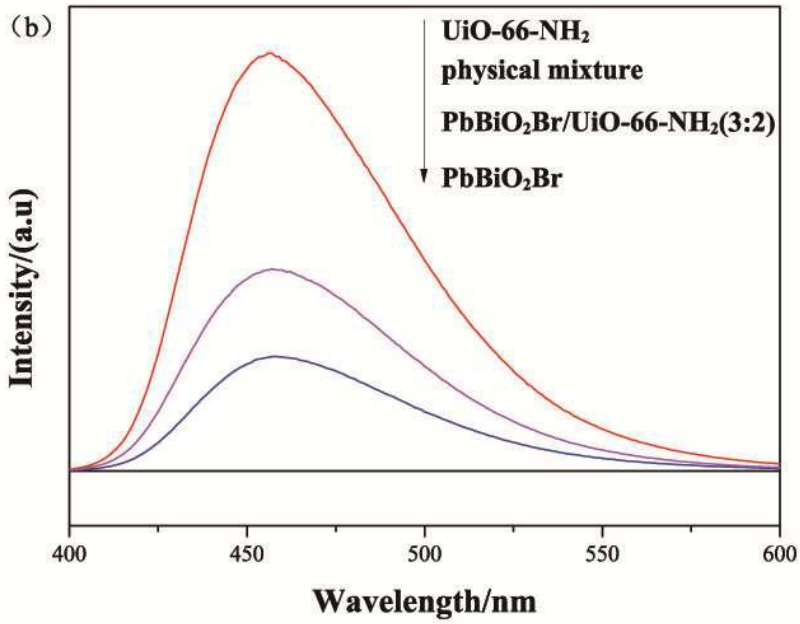

Fig. 5 (a) UV-vis absorption spectra of UiO-66-NH_2, $PbBiO_2Br$ and $PbBiO_2Br$/ UiO-66-NH_2 (3:2); (b) PL spectra of UiO-66-NH_2, $PbBiO_2Br$, physical mixture and $PbBiO_2Br$/ UiO-66-NH_2 (3:2).

3.2 Adsorption activity of $PbBiO_2Br/UiO\text{-}66\text{-}NH_2$ photocatalysts

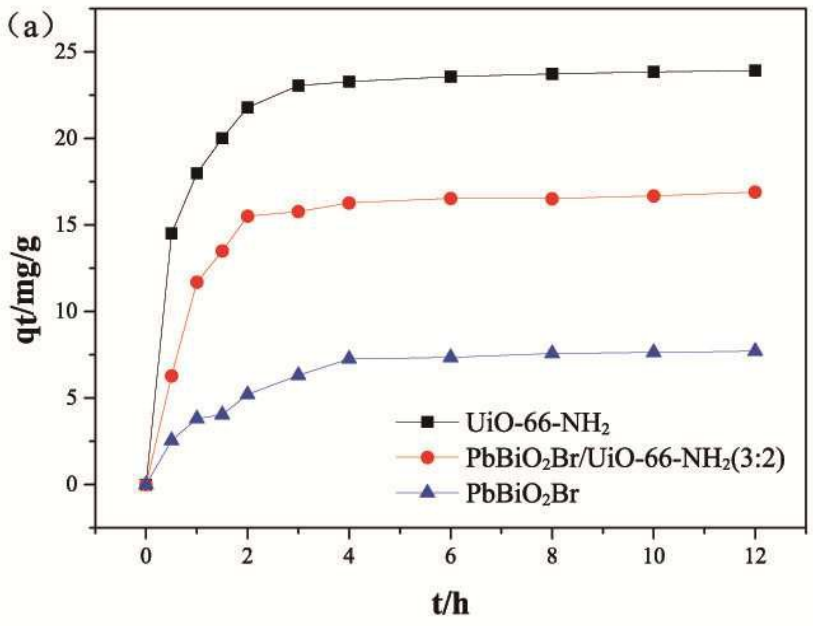

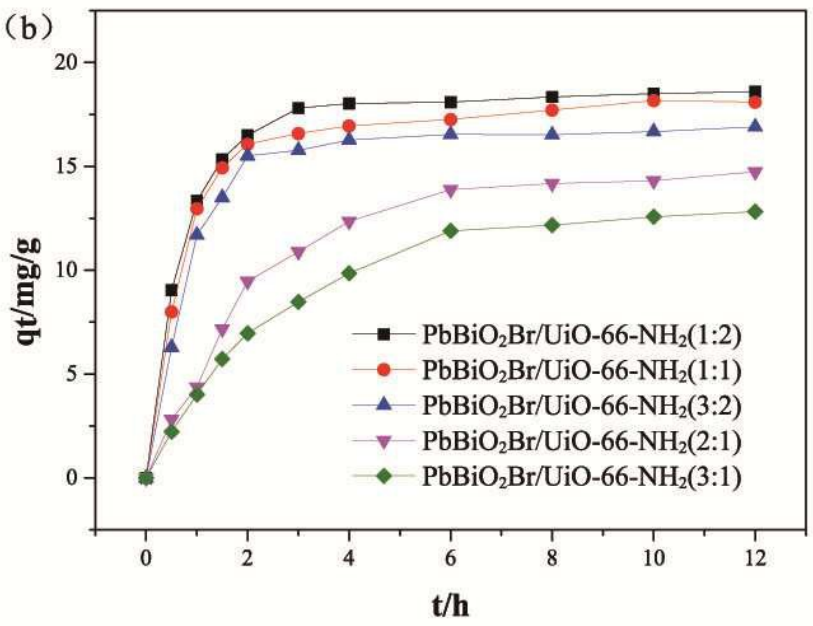

Fig. 6 (a) Adsorption capacity of RhB onto $PbBiO_2Br$, $UiO\text{-}66\text{-}NH_2$, and $PbBiO_2Br$ /

UiO-66-NH_2 (3:2); (b) Adsorption capacity of RhB on $PbBiO_2Br$ /UiO-66-NH_2 composites.

The adsorption performance of pure materials and composites was studied (Fig. 6). The adsorbed quantity, q_e, can be calculated using the following relationship:

$$q_e = \frac{V(C_0 - C_e)}{m} \quad \text{……..…..……....……... (2)}$$

where q_e (mg/g) is the amount of dye adsorbed onto the adsorbent at equilibrium, with C_0 and C_e (mg/L) denoting the liquid-phase concentrations of dye at initial and equilibrium, and *V (L)* and *m (g)* as the volume of dye solution and the mass of adsorbent, respectively.

$PbBiO_2Br$ displays low adsorption capacity of RhB in contrast with UiO-66-NH_2 and $PbBiO_2Br$ /UiO-66-NH_2 (3:2) (Fig. 6a). This is due to the big BET surface area and the mesopores structure of UiO-66-NH_2 and the electrostatic attraction interaction between RhB and UiO-66-NH_2 [34]. Meanwhile, the adsorption of RhB onto UiO-66-NH_2 has a great advantage as compared with that onto inorganic metal oxides such as $PbBiO_2Br$, because there exists various interactions like pi-pi stacking, hydrogen bonding, etc., between aromatic rings of RhB and UiO-66-NH_2. As shown in Figure 6a and 6b, the adsorption activities of the binary composites are between those of $PbBiO_2Br$ and UiO-66-NH_2, and increase with the increasing of UiO-66-NH_2 content.

3.3 Photocatalytic activity of UiO-66-NH_2, $PbBiO_2Br$ and the composites

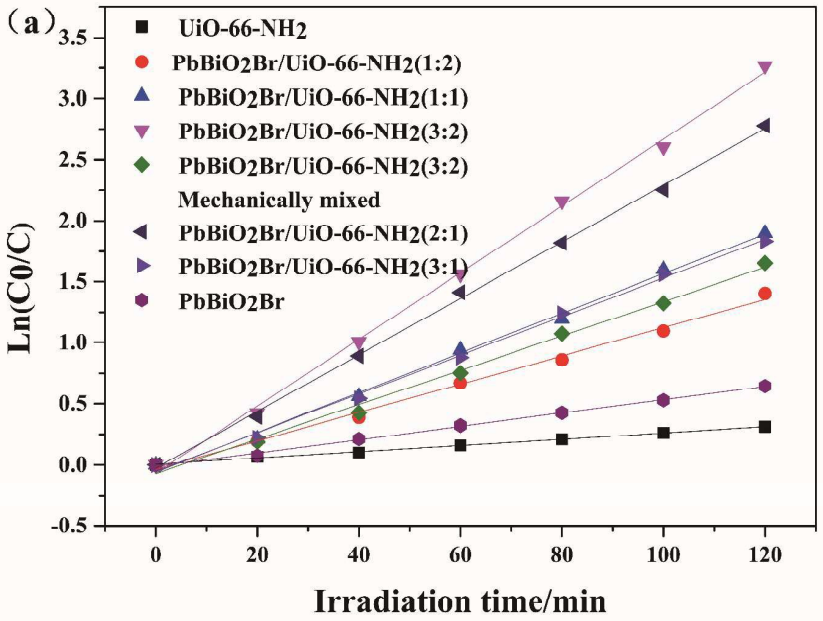

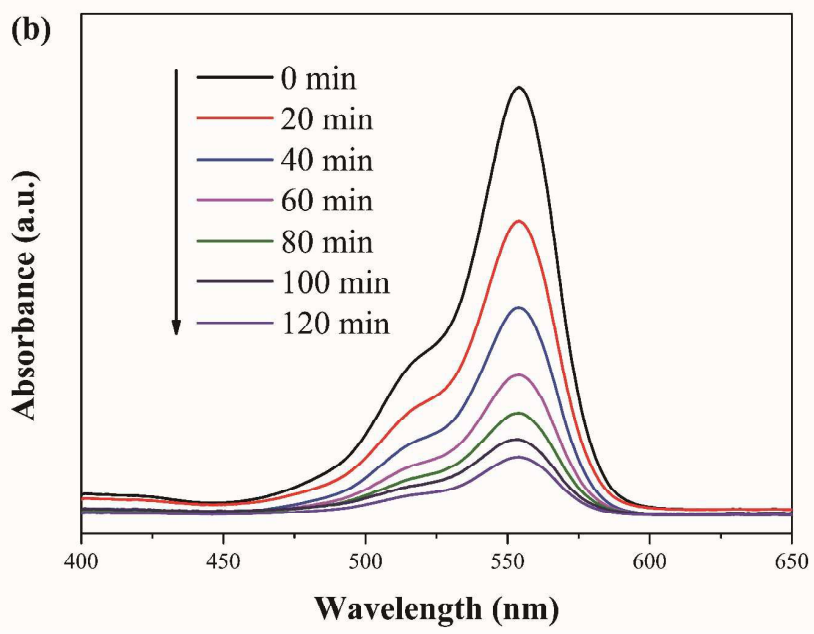

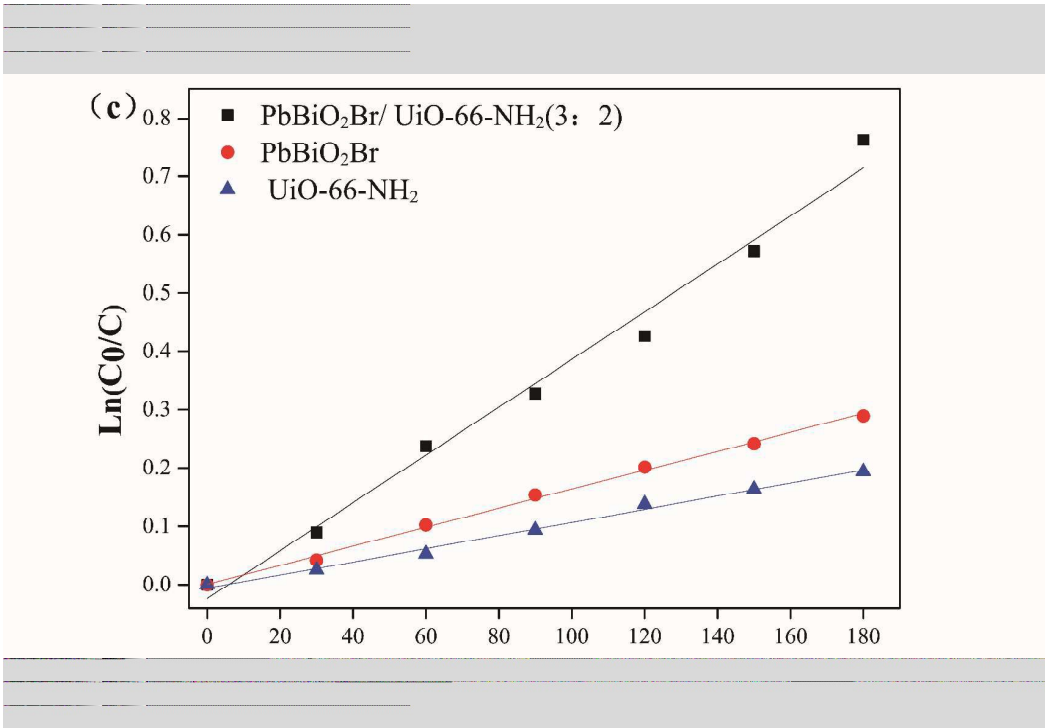

Fig. 7 (a) RhB degradation over various photocatalysts; (b) Absorption spectra of RhB after irradiation times in the presence of $PbBiO_2Br/UiO\text{-}66\text{-}NH_2$ (3:2) composite; (c) Photodegradation of phenol (5 mg/L) on $PbBiO_2Br$, $UiO\text{-}66\text{-}NH_2$, and $PbBiO_2Br/UiO\text{-}66\text{-}NH_2$(3:2).

The photocatalytic activities of $UiO\text{-}66\text{-}NH_2$, $PbBiO_2Br$ and the composites were evaluated using the degradation of RhB under visible light irradiation. Owing to small BET surface area of $PbBiO_2Br$ and poor separation efficiency of photogenerated electron-hole pairs of $UiO\text{-}66\text{-}NH_2$, both $PbBiO_2Br$ and $UiO\text{-}66\text{-}NH_2$ show low photocatalytic activity before compounding, as shown in Fig. 7(a) However, the $PbBiO_2Br$ /$UiO\text{-}66\text{-}NH_2$ composites exhibit a greatly enhanced photocatalytic activity, which may be due to the result of the combination of two different semiconductors.

The photocatalytic activities of $PbBiO_2Br/UiO\text{-}66\text{-}NH_2$ with differing

$PbBiO_2Br/ZrCl_4$ ratios were studied, and the results are displayed in Fig. 7(a). All the composites exhibit a higher photocatalytic activity than two pure components. In particular, the composite with the $PbBiO_2Br/ZrCl_4$ ratio at 3:2 displays the highest photocatalytic activity, and $PbBiO_2Br$ /UiO-66-NH_2(3:2) exhibits a higher photocatalytic activity than the mechanically mixed $PbBiO_2Br$ /UiO-66-NH_2(3:2) composites, which indicates that the synergistic effect between $PbBiO_2Br$ and UiO-66-NH_2 is the best [34]. As shown in Fig. 7(b), the absorption of RhB in the visible light region significantly decreased in the presence of $PbBiO_2Br$/UiO-66-NH_2 (3:2) composite. From this figure, the decrease of the characteristic absorption band of RhB at 552 nm can be obviously observed.

In addition, phenol is a colorless model organic pollutant, and the contribution of dye-sensitization during the degradation process could be ruled out. It was used as the second model pollutant to further evaluate the visible light photocatalytic performance of the as-prepared samples under visible light (λ < 380 nm was filtered out by a cut off filter), and the obtained results are illustrated in Fig. 7(c). It is also indicated that the $PbBiO_2Br$ /UiO-66-NH_2 (3:2) exhibits a higher photocatalytic activity than two pure components.

The regeneration of the photocatalyst is one of the important steps for practical applications. The stability of $PbBiO_2Br/ZrCl_4$ (3:2) was investigated, and after each photodegradation, it was separated from solution by centrifuge, and can be reused without considerable amount of mass loss. As shown in Figure 8a, after five cycles,

the K value stabilizes at about 0.245 min^{-1}, which is 89.74% of the first cycle. The good structural stability of $PbBiO_2Br/ZrCl_4$ (3:2) was further verified by XRD, as shown in Figure 8b.

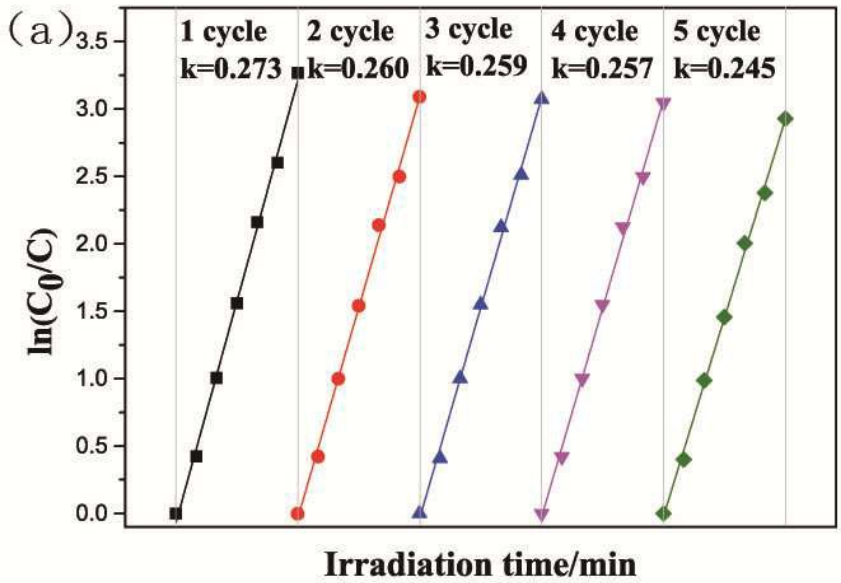

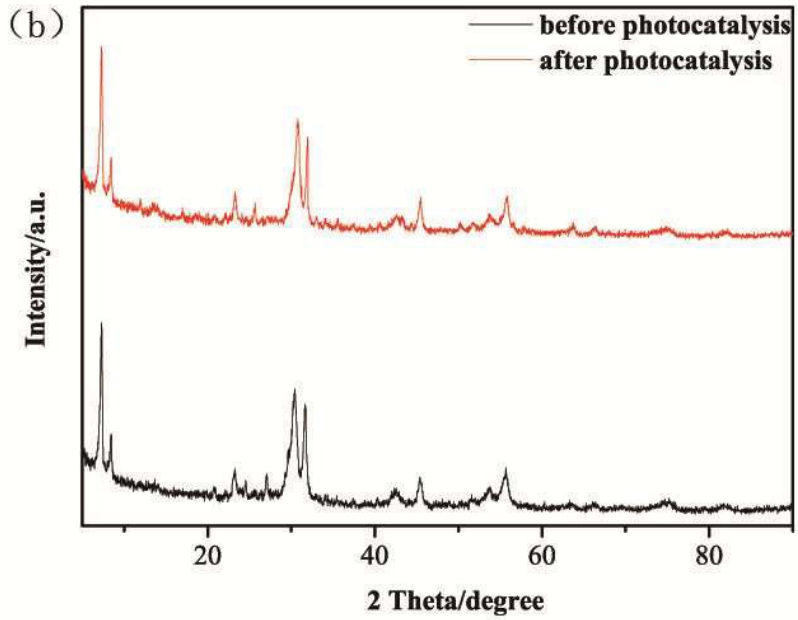

Fig. 8 (a) Kinetics and rate constant of RhB photodegradation on the recycled $PbBiO_2Br/UiO\text{-}66\text{-}NH_2$ (3:2); (b) XRD patterns of $PbBiO_2Br/UiO\text{-}66\text{-}NH_2$ (3:2) before and after photocatalysis.

3.4. Photodegradation Mechanism of RhB

In order to evaluate the role of various active oxidants, scavengers were added to the photocatalytic system. These are tert-butyl alcohol (t-BuOH) for •OH [35], benzoquinone (BQ) for $O_2^{\bullet -}$ [36] and disodium ethylenediaminetetraacetate dehydrate (EDTA-2Na) for the holes h^+ [37-39].

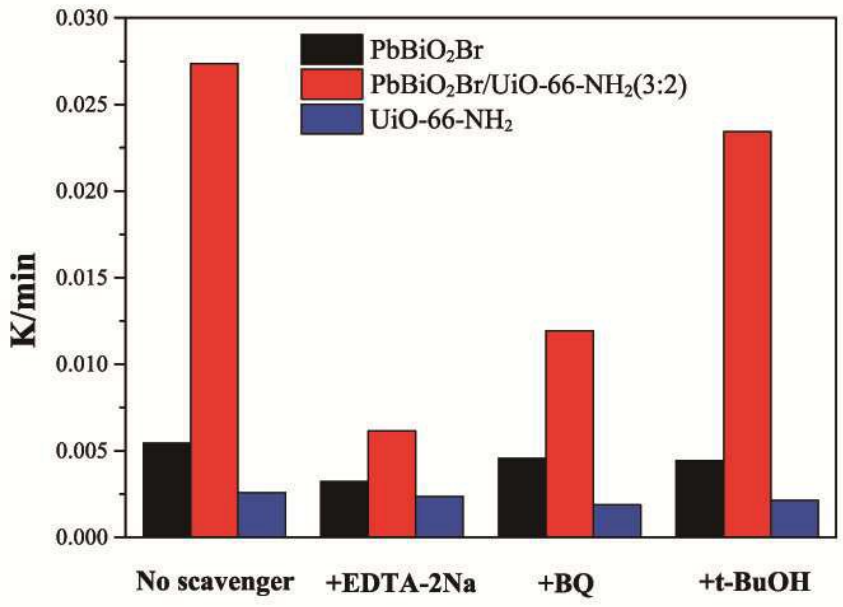

Fig. 9 The species trapping experiments for degradation of RhB over pure $PbBiO_2Br$, $UiO\text{-}66\text{-}NH_2$ and $PbBiO_2Br$/ $UiO\text{-}66\text{-}NH_2$ (3:2) photocatalysts under light irradiation.

The different active species trapping experiments for the degradation of RhB over the pure $PbBiO_2Br$, UiO-66-NH_2 and $PbBiO_2Br$/UiO-66-NH_2 (3:2) samples were first carried out to explore the enhancing photocatalytic mechanism. As shown in Fig. 9, for pure $PbBiO_2Br$, when EDTA-2Na, BQ and t-BuOH were added into reaction solution, the corresponding degradation rates of RhB decrease, and maintain at 59.27%, 83.85% and 81.1% of that of pure $PbBiO_2Br$, respectively, implying that the holes h^+ are the major reactive species. In contrast, the photodegradation kinetics constants only change a little for all species trapping experiments for pure UiO-66-NH_2. On the other hand, for the $PbBiO_2Br$/UiO-66-NH_2 (3:2) sample, when EDTA-2Na was added, the photocatalytic degradation rate decreases significantly, and only maintains at 22.45% of that without adding EDTA-2Na, indicating the holes h^+ are the predominant active species. When the BQ was added into reaction solution, the degradation rate of RhB is inhibited slightly (43.58%), suggesting $O_2\bullet^-$ also plays an important role in the photocatalytic process. When t-BuOH was added, the photocatalytic degradation rate basically keeps unchanged (85.63%), indicating that •OH plays a little role for the degradation of RhB. Therefore, the h^+ and $O_2\bullet^-$ radical are the major reactive species in the $PbBiO_2Br$/UiO-66-NH_2 (3:2) reaction system.

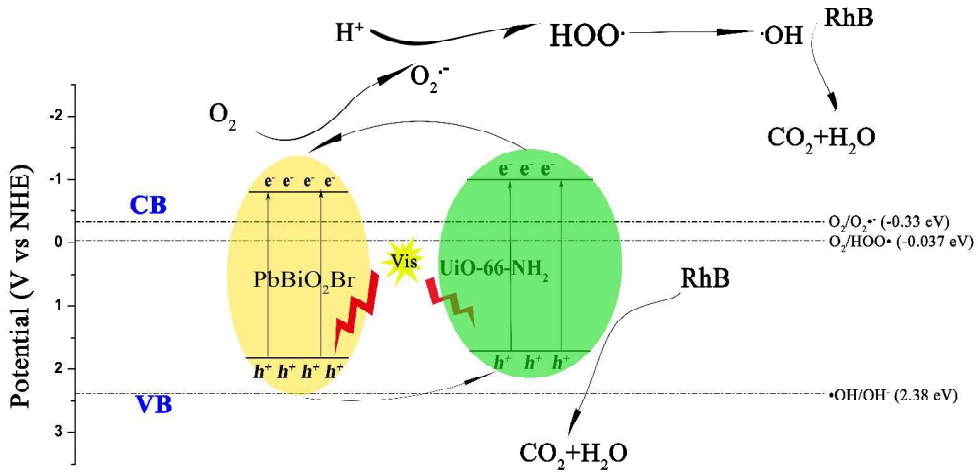

Fig. 10 Mechanism diagram of the RhB photodegradation on

$PbBiO_2Br/UiO\text{-}66\text{-}NH_2$

A photodegradation mechanism for the $PbBiO_2Br/UiO\text{-}66\text{-}NH_2$ composites under visible light irradiarion is shown in Fig.10. The conduction bands (CB) of $PbBiO_2Br$ and $UiO\text{-}66\text{-}NH_2$ are at -0.8 and -1.00[13, 40], respectively, which are more negative than the standard redox potential of $O_2/O_2\bullet^-$ (-0.33 eV) and O_2/HOO• (-0.037 eV) [41]. As a result, the photogenerated electrons in the CB of $PbBiO_2Br$ and $UiO\text{-}66\text{-}NH_2$ can reduce O_2 to give $O_2\bullet^-$ or HOO•, and the •OH radical can be generated from HOO• [42]. At the $PbBiO_2Br/UiO\text{-}66\text{-}NH_2$ heterojunction interface, the photogenerated electrons in the CB of $UiO\text{-}66\text{-}NH_2$ are transferred to the CB of $PbBiO_2Br$, and the holes from the valence band (VB) of $PbBiO_2Br$ are transferred to the VB of $UiO\text{-}66\text{-}NH_2$. Therefore, $UiO\text{-}66\text{-}NH_2$ can act as both an electron acceptor and donor. Hence, the electrons can easily migrate to the surface of $PbBiO_2Br$ and the redundant electrons on $PbBiO_2Br$ can also be transferred to $UiO\text{-}66\text{-}NH_2$. As a result, the

photogenerated electrons and holes are efficiently separated between $PbBiO_2Br$ and UiO-66-NH_2. And the UiO-66-NH_2 shell can enhance the adsorption of RhB cationic dye from the solution [43]. Thereby enhances the photocatalytic activity. The photogenerated electrons in the CB of $PbBiO_2Br$ including those from the CB of UiO-66-NH_2 can be captured by dissolved O_2 to yield first the superoxide radical anion, $O_2{\bullet}^-$, then the HOO• radical upon protonation, and finally the •OH radical via trapping the electron [42]. However, only small amount of the dye was oxidized by the •OH radical, and most of the dye was directly destroyed by the photogenerated holes in the VB of UiO-66-NH_2 including those from the VB of $PbBiO_2Br$. From Fig. 10, we can see that the electron-hole transfer at the $PbBiO_2Br$/UiO-66-NH_2 heterojunction interface enhances the separation of the electron-hole pairs [44]. Furthermore, after bringing together $PbBiO_2Br$ and UiO-66-NH_2, the resulting composites have the advantage of a high adsorption capacity especially for cationic dyes like RhB. These may be the reasons why the $PbBiO_2Br$/UiO-66-NH_2 composites have a synergistically enhanced photocatalytic performance as compared with the pure component materials.

4. Conclusions

In summary, $PbBiO_2Br$/UiO-66-NH_2 heterojunctions have been successfully prepared by a facile, one-pot solvothermal method. They have been investigated for the photodegradation of RhB dye solution and colorless phenol solution under visible light irradiation, and for two model organic pollutants, the heterojunctions all exhibits better photocatalytic activity than pure $PbBiO_2Br$ and UiO-66-NH_2. For RhB

degradation, the $PbBiO_2Br$/UiO-66-NH_2 (3:2) sample displays the highest degradation efficiency, the reaction rate of which is about 5 and 4 times as fast as that of $PbBiO_2Br$ and UiO-66-NH_2, respectively. In addition, photogenerated holes and $O_2^{\bullet -}$ radicals are believed to be the main active species responsible for photocatalysis.

Acknowledgement

This work was financially supported by the Anhui Provincial Natural Science Foundation (No.1508085MB28) and the National Natural Science Foundation of China (Grant. 51372062).

References

[1] A. S. Bhatt, P. L. Sakaria, M. Vasudevan, R. R. Pawar, N. Sudheesh, H. C. Bajaj, M. Mody, *RSC Advances,* **2012**, 2, 8663-8671.

[2] H. Chen, J. Zhao, *Adsorption*, **2009**, 15, 381-389.

[3] V. K. Gupta, B. Gupta, A. Rastogi, S. Agarwal, A. Nayak, *J. Hazard. Mater.*, **2011**, 186, 891-901.

[4] A. Dolbecq, P. Mialane, B. Keita, L. Nadjo, *J. Mater. Chem.*, **2012**, 22, 24509-24521.

[5] A. Kubacka, M. Fernández-García, G. Colón, *Chem. Rev.*, **2012**, 112, 1555-1614.

[6] W. Q. Fan, Q. H. Zhang, Y. Wang, *Phys. Chem. Chem. Phys.*, **2013**, 15, 2632-2649.

[7] Z. Yi, J. Ye, N. Kikugawa, T. Kako, S. Ouyang, H. Stuart-Williams, H. Yang, J. Cao, W. Luo, Z. Li, Y. Liu , R. L. Withers, *Nat. Mater.*, **2010**, 9, 559–564.

[8] L. Wu, H. B. Jiang, F. Tian, Z. Chen, C. Sun and H. G. Yang, *Chem. Commun.*, **2013**, 49, 2016–2018.

[9] J. Jiang, K. Zhao, X. Xiao and L. Zhang, *J. Am. Chem. Soc.*, **2012**, 134, 4473–4476.

[10] J. Ungelenk and C. Feldmann, *Chem. Commun.*, **2012**, 48, 7838–7840.

[11] N. Zhang, S. Ouyang, T. Kako and J. Ye, *Chem. Commun.*, **2012**, 48, 9894–9896.

[12] D. O. Charkin, P. S. Berdonosov, V. A. Dolgikh and P. Lightfoot, *J. Solid State Chem.*, **2003**, 175, 316–321.

[13] M. Cherevatskaya, M. Neumann, S. Fu¨ldner, C. Harlander, S. Ku¨mmel, S. Dankesreiter, A. Pfitzner, K. Zeitler and B. Ko¨nig, *Angew. Chem.*, *Int. Ed.*, **2012**, 51, 4062–4066.

[14] Z. C. Shan, W. D. Wang, X. P. Lin, H. M. Ding, F. Q. Huang, *J Solid State Chem*, **2013**, 3, 10687-10690.

[15] G. Q. Song, Z. Q. Wang, L. A. Wang, G. R. Li, M. J. Huang, F. X. Yin, *Chin J Catal.*,**2008**, 181, 1361-1366.

[16] G. Fe´rey, *Chem. Soc. Rev.*, **2008**, 37, 191-214.

[17] H. L. Li, M. Eddaoudi, M. O'Keeffe, O. M. Yaghi, *Nature*, **1999**, 402, 276-279.

[18] P. Wang, J. Feng, Y. P. Zhao, S. B. Wang, J. Liu, *ACS Appl. Mater. Interfaces*, **2016**, 8, DOI: 10.1021/acsami.6b08057.

[19] S. Kitagawa, R. Kitaura, S. I. Noro, *Angew. Chem. Int. Ed.*, **2004**, 43, 2334-2375.

[20] S. Hasegawa, S. Horike, R. Matsuda, S. Furukawa, K. Mochizuki, Y. Kinoshita, S. Kitagawa, *J. Am. Chem. Soc.*, **2007**, 129, 2607-2614.

[21] N. L. Rosi, J. Eckert, M. Eddaoudi, D. T. Vodak, J. Kim, M. O'Keeffe, O. M. Yaghi, *Science*, **2003**, 300, 1127-1129.

[22] M. Eddaoudi, J. Kim, N. Rosi, D. Vodak, J. Wachter, M. OÕKeeffe, O. M. Yaghi, *Science*, **2002**, 295, 469-472.

[23] M. Latroche, S. Surblé, C. Serre, C. Mellot-Draznieks, P. L. Llewellyn, J. H. Lee, J. S. Chang, S. H. Jhung, G. Férey, *Angew. Chem. Int. Ed.*, **2006**, 45, 8227-8231.

[24] P. Horcajada, C. Serre, M. Vallet-Regí, M. Sebban, F. Taulelle, G. Férey, *Angew. Chem.*, **2006**, 118, 6120-6124.

[25] C. G. Silva, I. Luz, F. X. Llabrés i Xamena, A. Corma, H. García, *Chem.-Eur. J.*, **2010**, 16, 11133-11138.

[26] T. W. Goh, C. X. Xiao, R. V. Maligal-Ganesh, X. L. Li, W. Y. Huang, *Chem. Eng. Sci.*, **2015**, 124, 45-51.

[27] L. Shen, W. Wu, R. Liang, R. Lin, L. Wu, *Nanoscale*, **2013**, 19, 9374-9382.

[28] M. A. Aramendía, V. Borau, J. C. Colmenares, A. Marinas, J. M. Marinas, J. A. Navío, F. J. Urbano, *Appl. Catal. B*, **2008**, 80, 88-97.

[29] M. Zhou, J. Yu, S. Liu, P. Zhai, L. Jiang, *J. Hazard. Mater.*, **2008**, 154, 1141-1148.

[30] F. Y. Xiao, J. Xing, Long. W, Z. P. Chen, X. L. Wang, H. G. Yang, *RSC advances*, **2013**, 3, 10687-10690.

[31] X. Zhang, F. Jia and L. Zhang, *J. Phys. Chem. C*, **2008**, 112, 747–753.

[32] X. F. Cao, L. Zhang, X. T. Chen, Z. L. Xue, *CrystEngComn*, **2011**, 13, 306-311.

[33] M. A. Butler, *J. Appl. Phys*, **1914**, 48, 1914-1920.

[34] Q. Chen, Q. Q. He, M. M. Lv, Y. L. Xu, H. B. Yang, X. T. Liu, F. Y. Wei, *Appl. Surf. Sci.*, **2015**, 327, 77-85.

[35] D. Chen; Z. Jiang; J. Geng; Q. Wang; D. Yang, *Ind. Eng. Chem. Res.*, **2007**, 46, 2741-2746.

[36] L. Mohapatra, K. Parida, M. Satpathy, *J. Phys. Chem. C*, **2012**, 116, 13063-13070.

[37] P. Xiong, Q. Chen, M. Y. He, X. Q. Sun, X. Wang, *J. Mater. Chem.*, **2012**, 22, 17485-17493.

[38] P. Xiong, L. J. Wan, X. Q. Sun, B. H. Xu, X. Wang, *Ind. Eng. Chem. Res.*, **2013**, 53, 10105-10113.

[39] Q. Chen, Q. Q. He, M. M. Lv, X. T. Liu□, J. Wang, J. P. Lv, *Appl. Surf. Sci.*, **2014**, 311, 230-238.

[40] X. Wang, S. O. Pehkonen and A. K. Ray, Ind. Eng. Chem. Res., **2004**, 43, 1665–1672.

[41] A. J. Bard, L. R. Faulkner, Electrochemical methods fundamentals and applications. John Wiley & Sons, New York, **1980**.

[42] T. X. Wu, G. M. Liu, J. C. Zhao, H. Hidaka, N. Serpone, *J. Phys. Chem. B*, **1998**, 102, 5845-5851.

[43] Q. Chen, Q. Q. He, M. M. Lv, Y. L. Xu, H. B. Yang, X. T. Liu, F. Y. Wei, *Appl. Surf. Sci.*, **2015**, 327, 77-85.

[44] J. M. Liu, Q. C. Zhang, J. C. Yang, H. Y. Ma, M. O. Tade, S. B. Wang, J. Liu, *Chem. Commun.*, 2014, 50, 13971-13974.